CAMBRIDGE
UNIVERSITY PRESS

Article

Physical properties and crystal structure of near end-member oxy-dravite from the Beluga occurrence, Nunavut territory, Canada

Lenka Skřápková[1], Jan Cempírek[1] , Philippe M. Belley[2], Lee A. Groat[3] and Radek Škoda[1]

[1]Department of Geological Sciences, Masaryk University, Kotlářská 2, 611 37 Brno, Czech Republic; [2]Department of Earth Sciences, Memorial University of Newfoundland, 9 Arctic Avenue, St. John's NL A1B 3X5, Canada; and [3]Department of Earth, Ocean and Atmospheric Sciences, University of British Columbia, Vancouver, British Columbia V6T 1Z4, Canada

Abstract

Oxy-dravite, ideally $Na(Al_2Mg)(Al_5Mg)(Si_6O_{18})(BO_3)_3(OH)_3(O)$, was found in a composition near its ideal end-member at the Beluga occurrence, Nunavut territory, Canada. It occurs in retrograde albite–muscovite–corundum–calcite domains in a calc-silicate rock. This uncommon oxy-dravite occurs as dark brown, equant to short-prismatic, idiomorphic crystals with vitreous lustre and up to ca. 4×3 cm in size. The oxy-dravite is optically uniaxial (–), with $\omega = 1.6453(5)$ and $\varepsilon = 1.6074(18)$; its calculated density is 3.069 g.cm^{-3} with a compatibility index of 0.016. The Beluga oxy-dravite has trigonal symmetry, space group $R3m$ with $a = 15.9121(2)$ Å, $c = 7.1788(10)$ Å, $V = 1574.12(5)$ Å^3 and $Z = 3$. The crystal structure was refined to $R_1 = 1.45$ using 1613 unique reflections. The empirical crystal-chemical formula is $^X(Na_{0.88}Ca_{0.08}\square_{0.03}K_{0.01})^Y(Al_{1.49}Mg_{1.31}Fe_{0.15}Ti_{0.04}Zn_{0.01})^Z(Al_{5.42}Mg_{0.58})^T(Si_{5.84}Al_{0.16}O_{18})^B(BO_3)_3$ $^V(OH_{2.95}O_{0.05})^W(O_{0.84}OH_{0.01}F_{0.15})$.

Oxy-dravite in nature commonly occurs in a solid solution with foitite, schorl and oxy-schorl. At the Beluga occurrence, its minor contents of Al, vacancy [$\square$], and Ca are most likely compensated by $(\square Al)(NaR^{2+})_{-1}$ and $(CaMg)(NaAl)_{-1}$ exchanges of the oxy-magnesio-foitite and magnesio-lucchesiite components. The Beluga occurrence of oxy-dravite is characterised by an Mg-rich environment related to a metamorphic overprint of the original sedimentary sequence. This sequence of marine dolomitic argillaceous marl was influenced by (B,Cl)-rich fluids, probably proximally-derived from mineral breakdown reactions in the calc-silicate during the retrograde stage of metamorphism. The locality is a rare example of a tourmaline + corundum assemblage.

Introduction

Tourmaline is a supergroup of minerals with general formula $XY_3Z_6[T_6O_{18}](BO_3)_3V_3W$, with primary occupancy: $X = Na^+$, Ca^{2+}, K^+ and $\square$ [vacancy]; $Y = Fe^{2+}$, Li^+, Al^{3+}, Mg^{2+}, Zn^{2+}, Cr^{3+}, Ti^{4+}, V^{3+} and Fe^{3+}; $Z = Al^{3+}$, Fe^{3+}, Mg^{2+}, Cr^{3+} and V^{3+}; $T = Si^{4+}$, Al^{3+} and B^{3+}; $B = B^{3+}$; $V = OH^-$ and O^{2-}; $W = OH^-$, F^- and O^{2-}. On the basis of the dominant X-site occupancy, tourmaline can be dived into the alkali group (Na), calcic group (Ca) and X-vacant group ($\square$). Each group is further divided, depending on the dominant occupancy of the W-site, into fluor-, hydroxyl- and oxy-subgroups (Henry *et al.*, 2011).

Oxy-dravite is an oxy-species, with oxygen as the dominant anion in the W-site, from the sodic group of the tourmaline supergroup of minerals (Henry *et al.*, 2011). Since its original description (Bosi and Skogby, 2013) from the quartz–muscovite schist from Osarara, Narok district, Kenya, the mineral has

been found at several localities worldwide, typically in metamorphic environments, and typically in solid solution with other species (e.g. Čopjaková *et al.*, 2012; Cempírek *et al.*, 2013; Pieczka *et al.*, 2018).

Although oxy-tourmalines are relatively new among the tourmaline species (e.g. Bosi and Skogby, 2013), their petrogenetic importance is significant. The tourmaline-supergroup minerals are widely regarded as a mineral that records a signature of the conditions and chemistry of its environment and, due to its high stability, preserves this signature (e.g. Henry and Dutrow, 1996). In primitive pegmatites, oxy-tourmaline shows distinct evolution of W-site occupancy between hydroxy- and oxy-species (Novák *et al.*, 2004). In marbles and calc-silicate rocks, oxy-tourmaline is shown to be a good monitor of fluctuations of fluid composition (Gadas *et al.*, 2014; Bosi *et al.*, 2017b; Krmíček *et al.*, 2021; Scribner *et al.*, 2021). Prior to its formal description, oxy-dravite was shown to be an indicator of metaevaporites (e.g. Henry *et al.*, 2008). In graphitic rocks, oxy-tourmaline records metamorphic reactions via episodic accumulation of Ti, Cr and V during its growth (Bosi *et al.*, 2013; Cempírek *et al.*, 2013; Bosi *et al.*, 2017a), and in ore systems, their increase of Fe^{3+} contents may indicate fluid

boiling and metal discharge (Duchoslav *et al.*, 2017; Drivenes 2022).

In this paper, we report the occurrence, and physical and structural properties of oxy-dravite with a near-end-member composition. These data improve characterisation of physical properties of oxy-dravite, allow examination of oxy-dravite solid solutions with respect to other species, improve the interpretation of Al–Mg disorder among the Y- and Z-sites, and discuss its petrogenetic importance.

Occurrence and paragenesis of oxy-dravite in the Beluga occurrence

The Beluga property is located in the southern part of Baffin Island, Nunavut territory, Canada (Fig. 1). The locality is known chiefly due to the occurrence of sapphire-bearing calc-silicate pods. These pods are hosted in a shelf sequence of clastic rocks and carbonates along with garnet-bearing metapsammite, metapelite, metasemipelite and rarely orthoquartzite of the Lake Harbour Group, a Paleoproterozoic supracrustal suite (Scott, 1997; Lepage and Rohtert, 2006; Corrigan *et al.*, 2009; Belley *et al.*, 2017; Belley and Groat, 2020). The Lake Harbour Group rocks, considered as a cover sequence of the Meta Incognita microcontinent, were transformed by several stages of metamorphism (granulite and amphibolite facies, 810°C/8 kbar and 720°C/8 kbar, respectively) during convergent orogenesis (initiated ca. 1849–1835 Ma) in the Trans-Hudson orogeny (St-Onge *et al.*, 2007). High-grade metamorphism was followed by final, localised retrograde overprints (ca. 1797–1785 Ma; St-Onge *et al.*, 2007). The area has diverse geology and is an excellent source of gemstones; sapphires, spinel (Belley and Groat, 2019) and lapis lazuli (Hogarth, 1971) occur in gem quality specimens.

At Beluga, uncommon oxy-dravite occurs as dark brown, equant to short-prismatic, idiomorphic crystals with maximal dimensions of ca. 4×3 cm (Fig. 2) in the retrograde albite–muscovite–corundum–calcite domains in the calc-silicate rock (Belley *et al.*, 2017). Belley *et al.* (2017) did not have sufficient textural evidence to clearly establish the associated stable mineral assemblage for oxy-dravite (i.e. either the prograde/peak metamorphic Di + Ne, high-temperature retrograde Phl + Pl + Scp, or the retrograde corundum-bearing assemblage; see Belley *et al.*, 2017 for details). However, additional field work at Beluga by Belley (2022 field season, unpublished) revealed the persistent, and seemingly exclusive, association of oxy-dravite with the retrograde corundum-bearing assemblage (albite–calcite–muscovite–corundum–graphite with accessory pyrrhotite). Oxy-dravite crystals observed in contact with corundum occur on the latter mineral's surface, conforming to the euhedral shape of corundum, and have not been observed as inclusions in corundum. Examination of 55 corundum crystals (Belley unpublished data, 2023) revealed common inclusions of calcite, three inclusions of phlogopite (partly altered to muscovite–amesite symplectites with subordinate V-bearing TiO_2) and one inclusion of scapolite. These inclusions may indicate that, at least in the early stages of mineralisation, corundum formed a stable assemblage with calcite–phlogopite–scapolite – forming earlier than previously estimated by Belley *et al.* (2017). Euhedral muscovite crystals occur on the surface of some corundum crystals and within fractures, thus it may not form a stable assemblage with the corundum. The textural relationships between corundum and oxy-dravite suggest that oxy-dravite probably formed simultaneously with, or later than, corundum.

The Beluga calc-silicate rock protolith is interpreted to be dolomitic marl (Belley *et al.*, 2017; Belley and Groat, 2019). Though the boron isotopic signature of the oxy-dravite is consistent with a marine boron source, this does not necessarily indicate that the Beluga rock consists of meta-evaporites. Evaporite-associated minor and trace elements, such as Mg, Mg/Ca ratio, B, B/Al ratio, Li, F and Cl, were not in concentrations sufficiently elevated as to indicate a definitive evaporitic signature (Belley *et al.*, 2017).

Experimental methods

The sample, a polished section of a crystal (ca. 6 mm in diameter) oriented perpendicular to the *c* axis, was analysed using a fully automated CAMECA SX-100 electron microprobe (EMP) in the Electron Microprobe Laboratory of the Department of Geological Sciences, Masaryk University (joint workplace of the Faculty of Science of Masaryk University and the Czech Geological Survey). The tourmalines were analysed in wavelength-dispersive mode, with accelerating voltage of 15 kV, beam current of 10 nA, and spot size of 5 μm. The following standards were used for measurement of major and minor elements in the tourmalines on $K\alpha$ X-ray lines: sanidine (Si, Al, K); albite (Na); pyrope (Mg); titanite (Ti); chromite (Cr); vanadinite (Cl); fluorapatite (P); wollastonite (Ca); almandine (Fe); spessartine (Mn); $ScVO_4$ (V); gahnite (Zn); and topaz (F). Average detection limits and 1σ for individual elements are, respectively (in wt.%): 0.043/ 0.201 (Na); 0.041/0.334 (Si); 0.035/0.424 (Al); 0.024/0.124 (Mg); 0.031/0.038 (Ti); 0.027/0.022 (Cr); 0.017/0.015 (Cl); 0.033/0.027 (P); 0.037/0.055 (Ca); 0.024/0.022 (K); 0.068/0.125 (Fe); 0.063/ 0.053 (Mn); 0.048/0.043 (V); 0.093/0.079 (Zn); and 0.053/0.05 (F). The Al/Si ratio was verified on a kyanite secondary standard.

The tourmaline formulae were calculated on the basis of T + Z + Y = 15 atoms per formula unit (apfu), assuming B = 3 apfu, full occupancy and Li at the Y site, zero [4]B at the T site, and OH = $(4 - {}^{V,W}O - F)$ (Henry *et al.*, 2011). All Fe was assumed to be divalent which is in agreement with bond-valence calculations. The assumption regarding Li is supported by the negligible Li contents detected by laser ablation inductively coupled plasma mass spectroscopy (LA-ICP-MS) analysis (<13 ppm). The tetrahedral bond length <T–O> ≈ 1.621 Å indicates full occupancy by Si or trace [4]Al at the T-site.

Trace-element analyses (Li, Be, B, P, Sc, Ti, V, Cr, Co, Ni, Cu, Zn, Ga, Y, Zr, REE, Th and U) were performed by LA-ICP-MS analysis at the Laboratory of Atomic Spectrochemistry of the Department of Chemistry (Faculty of Science, Masaryk University). The LA-ICP-MS equipment consists of an Analyte G2 (Teledyne CETAC Technologies) connected to a sector field ICP-MS spectrometer Element 2 (Thermo Fischer Scientific). An ArF* laser ablation device equipped with a HelEx II sample cell was operated at a wavelength of 193 nm. The ablated material was carried by He flow (0.65 L/min) and mixed with Ar (∼1 L/min) prior to entering the IC-PMS spectrometer. Optimisation of LA-ICP-MS parameters was performed with the glass reference material NIST SRM 610 with respect to the maximum signal-to-background ratio and $^{248}ThO^+/^{232}Th^+$ < 1. All element contents were normalised using Si determined from electron microprobe analysis (EMPA) as an internal standard. Data were processed using an in-house programmed optimisation spreadsheet in MS Excel. Analytical results and limits of detection (LOD) are reported in Table 1.
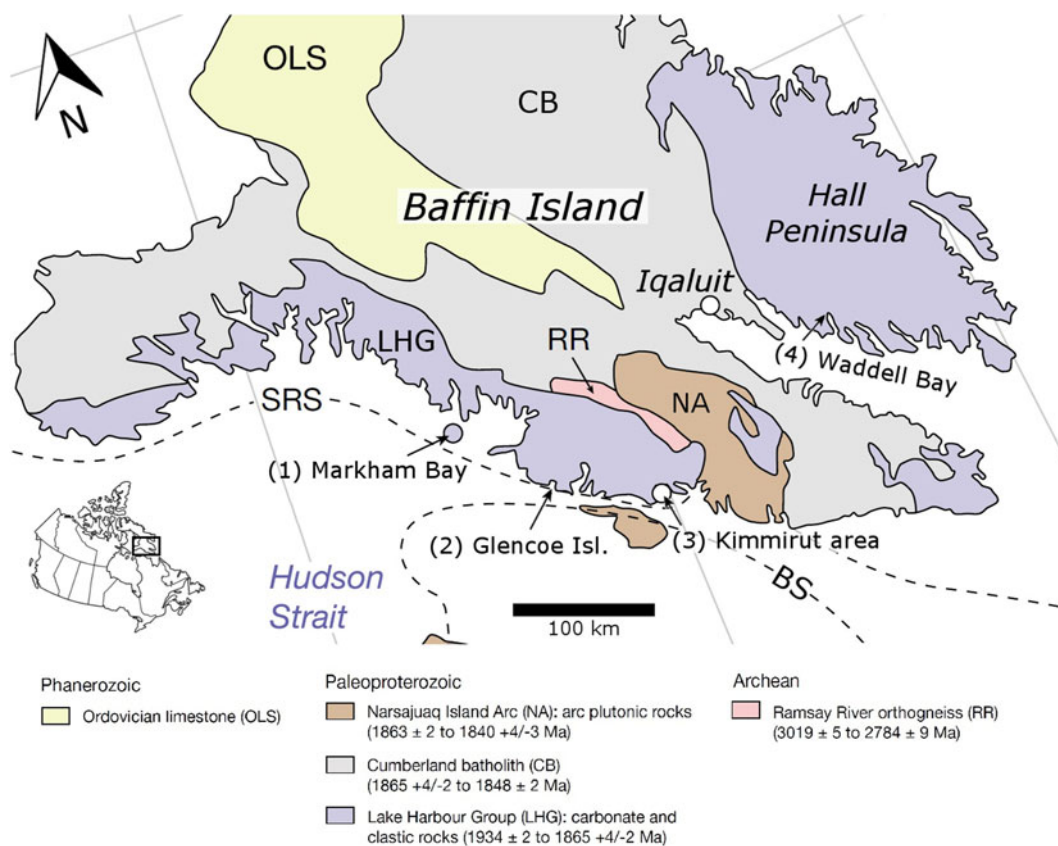
Figure 1. Geology of southern Baffin Island; the Beluga occurrence is located in the Kimmirut area (3), after Belley and Groat (2020).
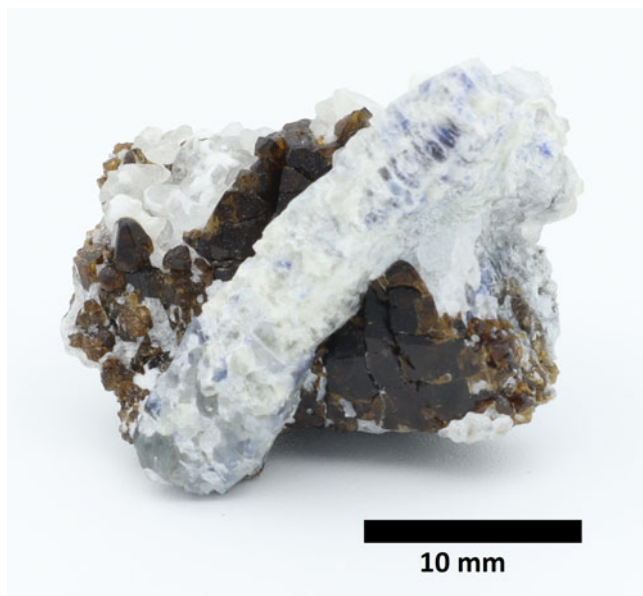

Figure 2. Photo of the sample containing the brown Beluga oxy-dravite in association with a prismatic light blue corundum crystal and late euhedral calcite (sample from collection of P. Belley).

The crystal structure of an oxy-dravite fragment extracted from the rim of the studied crystal was determined with a Bruker X8 APEX II diffractometer with graphite-monochromated MoKα radiation at C-HORSE (the Centre for Higher Order Structure Elucidation, in the Department of Chemistry at University of British Columbia). The crystal-to-detector distance was 40 mm. The data were collected at room temperature in a series of φ and ω scans in 0.50° oscillations with 10 s exposures (see Table 2). Data collection and integration was done using the Bruker *SAINT* software package (Bruker, 2007). Data were corrected for absorption effects using the multi-scan technique (*SADABS*, Sheldrick, 2008) and also for Lorentz and polarisation effects.

Polarised single-crystal Raman spectra of the Beluga oxy-dravite (rim of the polished section used for EMPA) were collected at room temperature using a Horiba LabRAM–HR spectrometer equipped with an Olympus BX41 optical microscope. The Raman signal was collected in the range of 100–4000 cm^{-1} using grating of 600 gr/mm and a 50× objective from four 60 s accumulations. The system was operated in the confocal mode with a beam diameter of ~1 μm. No visual damage to the analysed surface was observed after the excitation. Raman shift calibration was done using a Si wafer. The wavenumber accuracy was ~0.5 cm^{-1} and the spectral resolution was ~2 cm^{-1}. Band fitting was completed after appropriate background correction, assuming combined Lorentzian-Gaussian band shapes using the Voight function.

Chemical composition

The tourmaline sample is weakly zoned, with only minor changes from the crystal core to its rims (Fig. 3; Table 2). The X-site is occupied predominantly by Na (0.87 to 0.91 apfu), its Ca content

Table 1. Selected representative chemical compositions of the Beluga oxy-dravite (rim to core profile across a large crystal using EMPA and LA-ICP-MS, and the EMPA composition of the crystal used for SC-XRD).

Analysis no.	1 (rim)	4	5	7 (core)	SC-XRD
EMPA data (wt.%)					
SiO_2	36.61	35.36	36.05	36.83	36.18
TiO_2	0.46	0.04	b.d.l.	0.40	0.36
B_2O_3*	10.70	10.73	10.79	10.85	10.76
Al_2O_3	35.90	38.26	38.30	36.63	37.10
MgO	8.20	7.34	7.94	8.29	7.84
FeO	0.97	1.33	1.33	1.08	1.14
ZnO	0.04	b.d.l.	0.08	0.02	0.02
CaO	0.27	0.68	0.53	0.19	0.46
Na_2O	2.83	2.78	2.79	2.93	2.82
K_2O	0.02	0.05	0.03	0.02	0.04
F	0.34	0.26	0.24	0.32	0.30
H_2O*	2.73	2.74	2.72	2.84	2.74
−O=F	−0.14	−0.11	−0.10	−0.14	−0.13
Total	99.00	99.49	100.00	100.31	99.67
Normalised to Y + Z + T = 15 apfu					
Si^{4+}	5.945	5.730	5.807	5.901	5.844
Ti^{4+}	0.057	0.005	b.d.l.	0.048	0.044
B^{3+}	3.000	3.000	3.000	3.000	3.000
Al^{3+}	6.869	7.307	7.272	6.917	7.063
Fe^{2+}	0.132	0.181	0.179	0.145	0.154
Zn^{2+}	0.004	b.d.l.	0.009	0.003	0.002
Mg^{2+}	1.984	1.774	1.728	1.980	1.887
Ca^{2+}	0.047	0.118	0.091	0.033	0.080
Na^+	0.890	0.873	0.870	0.910	0.884
K^+	0.004	0.011	0.007	0.003	0.007
F^-	0.172	0.131	0.124	0.162	0.151
OH^-	2.960	2.961	2.921	3.033	2.951
O^{2-}	0.868	0.907	0.955	0.803	0.897
LA-ICP-MS data (ppm)					LOD
Ti	3324	246	308	3734	1.10
Sc	5.71	4.48	4.11	6.15	0.14
V	221	106	104	210	0.01
Cr	2.31	3.73	2.93	10.18	0.17
Li	10.87	8.94	8.60	8.04	0.28
Ga	62.35	63.15	56.79	69.05	0.02
Mn	26.48	40.48	36.97	25.90	0.18
Co	1.95	3.00	2.80	1.91	0.02
Ni	2.85	5.66	4.78	3.00	0.09
Zn	24.47	30.44	26.69	23.37	0.13

Note: b.d.l – below detection limit; LOD – limits of element detection for LA-ICP-MS data; SC-XRD – single-crystal X-ray diffraction.
*calculated from stoichiometry, see Methods.

Table 2. Crystal data, data collection and refinement parameters for near end-member oxy-dravite from Beluga.

Crystal data	
a (Å)	15.9121(2)
b (Å)	15.9121(2)
c (Å)	7.1788(1)
V (Å^3)	1574.12(5)
Z	3
Crystal size (mm)	0.15 × 0.10 × 0.09
Crystal shape, colour	anhedral, brown
Crystal system, space group	Trigonal, $R3m$
Data collection	
Diffractometer	Bruker X8 APEX II
Scan method	φ, ω
Temperature (K)	296
Radiation Mo$K\alpha$ (Å)	0.71073
μ (mm^{-1})	1.42
F(000)	1627
Range for data collection, θ (°)	2.56−35.04
h, k, l ranges	−25/25, −25/25, −10/11
Total reflections measured	19234
Unique reflections	1650
Reflections used for determination of unit-cell parameters	1650
R_{int} (%)	3.12
Refinement	
R_1 (%)	1.47
R_1 (%) for $[F^2 > 2\sigma(F^2)]$	1.54
$wR(F^2)$	0.035
GoF (S)	1.067
Largest diff. peak and hole (e^-/Å^3)	0.27 and −0.34

Crystal structure and bond valence refinement

The crystal structure of the oxy-dravite sample was refined from single-crystal X-ray diffraction data. The refinements were performed using the *SHELXTL* crystallographic software package (Sheldrick, 2008, 2015) of Bruker AXS. Scattering factors for neutral atoms were employed for the cations and ionic factors for O^{2-} were used for oxygen (Hovestreydt, 1983). The structure of dravite after Foit and Rosenberg (1979) was introduced as an initial model for refinement that was processed (by refining occupancy of Na at the X-site, and Fe *vs.* Al at the Y- and Z-sites) to a final *R* index of ∼1.45% for an anisotropic displacement model. The H3-atom site was located in residual electron-density maps whereas the H1 site was impossible to locate. The H3 site isotropic displacement parameter was constrained to be equal to 1.2 times of that of the O3 site; its distance from the donor oxygen atom was constrained to 0.92(2) Å.

The mean <Z−O> bond length of 1.928 Å indicates that the Z-site is not fully occupied by Al (ideally <^{Z}Al−O> = 1.906 Å; Bosi and Andreozzi, 2013) but partially replaced by Mg, suggesting ^{Y,Z}(Al−Mg) disorder. Occupancies of octahedral sites were refined using bond-valence optimisation (Table 3) which confirmed disorder of Mg and Al between the Y- and Z-sites, typical for Mg-rich tourmalines (e.g. Grice and Ercit, 1993; Hawthorne *et al.*, 1993; Ertl *et al.*, 2003; Bosi and Lucchesi, 2004; Bosi and Skogby, 2013; Bačík, 2015; Pieczka *et al.*, 2018; Scribner *et al.*, 2021; Bosi *et al.*, 2022; Sęk *et al.*, 2022).

The occupancy of the T-site is dominated by Si but its content varies: 5.73−5.95 apfu. With the elongated <T−O> bond length, it is evident that some amount of Al^{3+} (or, less likely, a combination of $Al^{3+} + B^{3+}$) is present in the T-site (e.g. Grice and Ercit, 1993;

varies from 0.03 to 0.12 apfu, and vacancy contents are negligible (<0.06 pfu). The V- and W-sites are characterised by high OH (2.92−3.00 apfu) and O contents (0.80−0.95 apfu), with minor F (0.12−0.17 apfu) only.

The octahedral Y- and Z-sites contain dominant Al (6.87−7.31 apfu) and contain high Mg (1.73−1.98 apfu), and low contents of Fe^{2+} (0.13−0.18 apfu); Li is negligible (<13 ppm based on LA-ICP-MS). The tetrahedral site is occupied mostly by Si (5.73−5.95 apfu) with minor substituted Al (0.06−0.27 apfu).

Amounts of trace elements determined by LA-ICP-MS analyses are generally very low (Table 1 − EMPA and LA-ICP-MS). The only exceptions are Ti and V with maximum values up to 4495 ppm (up to 0.75 wt.% TiO_2) and 312 ppm (0.05 wt.% V_2O_3), respectively; they show a slight decrease from the crystal rims towards the core. Contents of Sc, P, Li, Cr, Mn, Co, Ni, Ga and Zn are close to their detection limits and approach tens of ppm in maximum values. The amounts of REE, Be, Cu and Zr are below their detection limits.
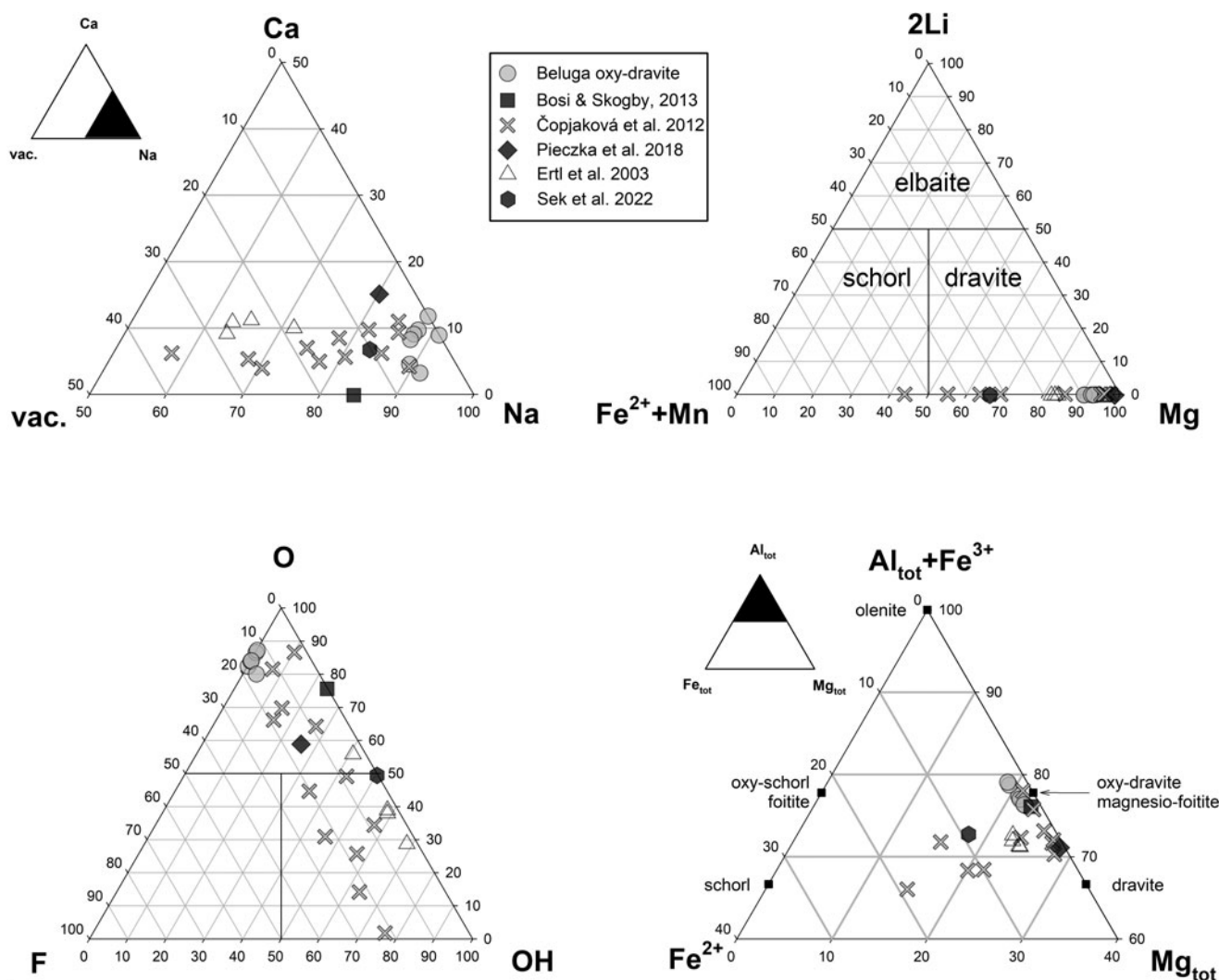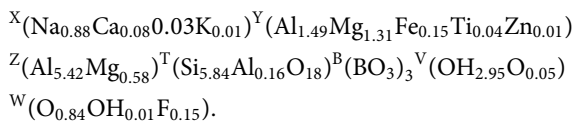
Figure 3. Composition of the Beluga oxy-dravite in several compositional spaces compared to compositions from other studies (Ertl *et al.*, 2003; Čopjaková *et al.*, 2012; Bosi and Skogby, 2013; Pieczka *et al.*, 2018; Sęk *et al.*, 2022). Note the high miscibility with vacancy-, Fe- and OH-dominated species.

MacDonald and Hawthorne, 1995; Hawthorne, 2002; Ertl *et al.*, 2018). The final empirical structural formula, with hydrogen distribution adjusted between the V- and W-sites, using the formula of Bosi (2013), is:

$$^X(Na_{0.88}Ca_{0.08}\square_{0.03}K_{0.01})\,^Y(Al_{1.49}Mg_{1.31}Fe_{0.15}Ti_{0.04}Zn_{0.01})$$
$$^Z(Al_{5.42}Mg_{0.58})\,^T(Si_{5.84}Al_{0.16}O_{18})\,^B(BO_3)_3\,^V(OH_{2.95}O_{0.05})$$
$$^W(O_{0.84}OH_{0.01}F_{0.15}).$$

For the final step of the structure refinement, atom fractions from the final empirical formula were fixed to the individual sites; final bond lengths (rare changes on third decimal place) were used again for the bond-valence optimisation (using values R_0 and B from Gagné and Hawthorne, 2015) which resulted in results identical to the previous step. Final atomic parameters and refined scattering values expressed as site occupancies are given in Table 4 and selected interatomic distances in Table 5. The crystallographic information file has been deposited with the Principal Editor of *Mineralogical Magazine* and is available as Supplementary material (see below).

Physical properties

The Beluga oxy-dravite is strongly pleochroic, light yellowish-brown colour in the omega direction and colourless in the epsilon direction. The Beluga oxy-dravite is uniaxial (−) with $\omega = 1.6453(5)$ and $\varepsilon = 1.6074(18)$, measured using a low pressure Na-vapour lamp. The density calculated using the observed cell volume and the empirical composition is 3.069 g.cm^{-3}. The compatibility index reflecting the difference between the physical (K_p) and the chemical specific-refractivity (Mandarino, 1981) is 0.016, corresponding to the superior category. A comparison of the Beluga oxy-dravite optical properties with those for other tourmaline Mg-bearing end-members is shown in Table 6.

Raman spectra

The Raman spectrum of the Beluga oxy-dravite (Fig. 4) was (after background correction) fitted using Pseudo-Voight peaks. The spectrum pattern generally corresponds well to that of oxy-dravite and other Mg-bearing tourmalines (Watenphul *et al.*, 2016a, 2016b; Watenphul *et al.*, 2017). According to the equations provided by Watenphul *et al.* (2016b), there is a dependence

Table 3. Fractional atomic coordinates, isotropic/equivalent isotropic displacement parameters (Å^2), and anisotropic atomic displacement parameters (Å^2).

Site	x	y	z	Site occupancy	U_{iso}*/U_{eq}
T	0.47694(2)	0.33524(2)	0.69959(5)	Si$_1$	0.00440(8)
Z	0.40543(3)	0.36955(3)	0.30952(6)	Al$_{0.89(5)}$Mg$_{0.11(5)}$	0.0046(2)
Y	0.60522(2)	0.39478(2)	0.33532(9)	Mg$_{0.915(4)}$Fe$_{0.085(4)}$	0.00661(18)
X	0.3333	0.6667	0.2609(2)	Na$_{1.058(8)}$	0.0214(5)
B	0.44300(7)	0.55700(7)	0.4864(3)	1	0.0057(3)
O1	0.6667	0.3333	0.4691(4)	O$_{0.93(6)}$F$_{0.07(6)}$	0.0109(7)
O2	0.39387(5)	0.60613(5)	0.5192(2)	1	0.0091(3)
O3	0.53607(6)	0.46393(6)	0.2094(2)	1	0.0126(3)
O4	0.47966(11)	0.23983(6)	0.7721(2)	1	0.0096(2)
O5	0.57457(5)	0.42543(5)	0.7933(2)	1	0.0091(2)
O6	0.48266(7)	0.34361(7)	0.47591(15)	1	0.00712(17)
O7	0.38148(6)	0.33371(7)	0.77719(14)	1	0.00703(17)
O8	0.39408(7)	0.45742(7)	0.47191(14)	1	0.00796(17)
H3	0.5443(11)	0.4557(11)	0.085(3)	1	0.015*

Site	U^{11}	U^{22}	U^{33}	U^{12}	U^{13}	U^{23}
T	0.00392(13)	0.00406(13)	0.00510(15)	0.00189(11)	0.00056(11)	0.00024(10)
Z	0.0047(2)	0.0048(2)	0.0046(3)	0.00248(16)	−0.00029(12)	−0.00061(12)
Y	0.0040(2)	0.0040(2)	0.0106(3)	0.00099(19)	0.00206(9)	−0.00206(9)
X	0.0216(6)	0.0216(6)	0.0210(9)	0.0108(3)	0.000	0.000
B	0.0051(5)	0.0051(5)	0.0069(8)	0.0025(6)	0.0000(3)	0.0000(3)
O1	0.0134(9)	0.0134(9)	0.0061(12)	0.0067(4)	0.000	0.000
O2	0.0115(5)	0.0115(5)	0.0094(7)	0.0097(5)	0.0001(2)	−0.0001(2)
O3	0.0125(4)	0.0125(4)	0.0037(6)	−0.0006(5)	0.0001(3)	−0.0001(3)
O4	0.0150(6)	0.0074(4)	0.0088(6)	0.0075(3)	0.0016(5)	0.0008(3)
O5	0.0068(4)	0.0068(4)	0.0086(6)	−0.0006(4)	−0.0009(2)	0.0009(2)
O6	0.0088(4)	0.0076(4)	0.0044(4)	0.0037(3)	0.0013(3)	0.0006(3)
O7	0.0055(4)	0.0100(4)	0.0067(4)	0.0046(3)	0.0010(3)	−0.0003(3)
O8	0.0063(4)	0.0042(4)	0.0115(4)	0.0012(3)	0.0020(3)	−0.0005(3)

Table 4. Bond distances of the crystal studied (Å).*

X–O2 (×3)	2.4941(19)	Z–O8	1.8971(10)
X–O5 (×3)	2.7152(16)	Z–O6	1.9012(11)
X–O4 (×3)	2.8084(17)	Z–O7^{iv}	1.9017(10)
<X–O>	2.673	Z–O8^{v}	1.9212(10)
		Z–O7^{v}	1.9518(10)
Y–O1	1.9469(14)	Z–O3	1.9929(8)
Y–O6 (×2)	1.9741(11)	<Z–O>	1.928
Y–O2 (×2)	1.9944(10)		
Y–O3	2.1093(18)	T–O7	1.6066(9)
<Y–O>	1.999	T–O6	1.6101(11)
		T–O4	1.6259(6)
B–O8 (×2)	1.3763(14)	T–O5	1.6419(7)
B–O2	1.3740(20)	<T–O>	1.621
<B–O>	1.376		

*Symmetry codes: (iv) –y+⅔, x–y+⅓, z–⅔; (v) –x+y+⅓, –x+⅔, z–⅓

of measured ω(ZO$_6$) (ω = Raman shift) on the content of non-aluminium cations (Mg and Fe^{3+}) at the Z-site. The calculated values for the Beluga oxy-dravite are 0.98(19) apfu ^{Z}Mg and 0 apfu ^{Z}Fe^{3+}; the error of the calculated ^{Z}Mg value overlaps with the error of the structurally refined ^{Z}Mg value (0.66±0.30 apfu). Despite the large difference, the result shows that the Raman calculation above is a valid tool for estimation of ^{Y,Z}Mg disorder.

The Beluga oxy-dravite Raman peaks related to OH at the W-site (range 3711–3772 cm^{-1}) generally agree with data described by Watenphul *et al.* (2016a). The most intense peak at 3739 cm^{-1} is related to the ^{Y}Mg^{Y}Mg^{Y}Al–^{X}Na configuration of atoms around the O1 atom whereas the peak at 3772 cm^{-1} matches values reported for the ^{Y}Mg^{Y}Mg^{Y}Mg–^{X}Na configuration

in dravite and uvite (Watenphul *et al.*, 2016a). For the peak at 3711 cm^{-1} we propose the configuration ^{Y}Mg^{Y}Al^{Y}Al–^{X}Na as it must be present in a significant amount due to the Mg–Al disorder between the Y- and Z-sites revealed by the structural refinement (below). The presence of peaks related to ^{W}OH indicates that the ^{V}OH must be present in a significant amount. In the disorder calculation (Bosi, 2013), ^{W}OH is negatively correlated to F content; the Raman results may suggest slight fluorine overestimation, possibly due to use of topaz as an EMPA standard (Ottolini *et al.*, 2000).

By comparison with Raman spectra of dravite (Watenphul *et al.*, 2016a), the two most intense ^{V}OH-peaks of the Beluga oxy-dravite at 3531 and 3574 cm^{-1} (Fig. 4) probably correspond to the 2^YMg^{Z}Al^{Z}Al–^{Y}Al^{Z}Al^{Z}Al, and 3^YMg^{Z}Al^{Z}Al configurations, respectively. The middle peak at 3556 cm^{-1} is closest to the 2^YMg^{Z}Mg^{Z}Al–^{Y}Mg^{Z}Al^{Z}Al configuration (located at 3547 cm^{-1} in uvite; Watenphul *et al.*, 2016a) which corresponds with Mg–Al disorder between the Y- and Z-sites. Peaks at similar wavenumbers (3548–3560 cm^{-1}) were observed by Fantini *et al.* (2014) in dravite, magnesio-foitite and uvite.

Discussion

Comparison of reported oxy-dravite compositions and structures

Tourmaline with oxy-dravite composition has been described from multiple occurrences (Ertl *et al.*, 2003; Čopjaková *et al.*, 2012; Bosi and Skogby, 2013; Pieczka *et al.*, 2018; Sęk *et al.*, 2022). Its composition typically deviates from the ideal end-member by elevated amounts of Fe and vacancies (e.g. Novák

Table 5. Empirical weighted bond valences (in valence units) and other structural site parameters for the Beluga oxy-dravite.*

Site	X	Y	Z	T	B	Σ_{anion}
O1	–	$0.45^{\times 3}\rightarrow$	–	–	–	1.34
O2	$0.15^{\times 3}\downarrow$	$0.41^{\times 2}\downarrow^{\times 2}\rightarrow$	–	–	0.99	1.97
O3	–	$0.31^{\times 2}\rightarrow$	0.40	–	–	$2.10^{\S}$
O4	$0.07^{\times 3}\downarrow$	–	–	$1.00^{\times 2}\rightarrow$	–	2.06
O5	$0.09^{\times 3}\downarrow$	–	–	$0.96^{\times 2}\rightarrow$	–	2.00
O6	–	$0.43^{\times 2}\downarrow$	0.50	1.04	–	1.98
O7	–	–	0.50, 0.44	1.05	–	1.99
O8	–	–	0.51, 0.48	–	$0.99^{\times 2}\downarrow$	1.98
Σ_{cation}	0.95	2.45	2.84	4.03	2.97	
Mean formal charge	1.05	2.53	2.90	3.97	3.00	
Sums:						
mean atomic number (obs.)	11.64(9)	13.19(6)	12.89(5)	14	5	227.58
mean atomic number (cal.)	11.46	13.38	12.89	13.97	5	227.77

*Note: obs. = observed; cal. = calculated. §Includes 0.99 valence units contribution from H3.

Table 6. The comparison of oxy-dravite optical properties with other tourmaline Mg-bearing end-members.

	Beluga	Bosi and Skogby (2013)	mindat.org*	Clark *et al.* (2011)	Bosi *et al.* (2022)	Scribner *et al.* (2021)
	oxy-dravite	oxy-dravite	dravite	fluor-dravite	uvite	magnesio-lucchesiite
Ω	1.6453(5)	1.650(5)	1.634–1.661	1.645(2)	1.660(5)	1.668
E	1.6074(18)	1.620(5)	1.612–1.632	1.621(2)	1.640(2)	1.644
Colour	dark brown	dark red	pale to dark brown to brownish-black, dark-yellow, blue	blackish brown	brown	brownish to bluish
Pleochroism	O = yellowish brown	O = orange	O = pale yellow	O = pale yellowish brown	O = greenish brown	O = dark brown
	E = colourless	E = pink	E = colourless, yellowish, greenish, brownish	E = colourless	E = pale yellow	E = colourless to dark brown
Density (calc.) (g.cm^{-3})	3.069	3.073	3.038	3.120	3.115	3.168
Compatibility index (K_p)	0.016	0.028	–	0.030	0.023	0.034

*https://www.mindat.org/min-1318.html

et al., 2004; Čopjaková *et al.*, 2012; Bosi *et al.*, 2013), or Ca (e.g. Pieczka *et al.*, 2018). The vacancy and Fe contents result mainly from foitite, oxy-schorl, or schorl components due to the substitutions ($\square$FeOH)(NaMgO)$_{-1}$, Fe$_1$Mg$_{-1}$, and (Fe$_3$OH)(Mg$_2$AlO)$_{-1}$, respectively. The oxy-dravite from Beluga shows a slight excess (Al$_{tot}$ = 7.06 apfu) of Al, which might indicate substitution to 'oxy-magnesio-foitite' via the ($\square$Al)(NaR^{2+})$_{-1}$ mechanism analogous to the schorl–foitite transition (e.g. Novák *et al.*, 2004). The slightly elevated Ca-content is most likely to be compensated by the (CaMg)(NaAl)$_{-1}$ exchange (magnesio-lucchesiite component). The compositional shift from dravite/fluor-dravite to oxy-dravite can be expressed by the substitution (MgOH/F)$_{-1}$ (AlO) (Bačík *et al.*, 2012; Fig. 5).

Data from studies of Bosi and Skogby (2013) and Sęk *et al.* (2022) plot in the oxy-dravite field (Fig. 5b); however, samples in both of those studies contain significant amounts of Fe^{3+} (0.610 apfu and 0.565 apfu, respectively). Adjustment of the ^{Y}Al^{3+} values to ^{Y}R^{3+} (which considers ^{Y}Fe^{3+}) justifies their classification as oxy-dravite, at least in the case of the holotype described by Bosi and Skogby (2013). Sęk *et al.* (2022) correctly considered dravitic to oxy-dravitic compositions with significant Fe^{3+} component.

In comparison with other data on oxy-dravite (Ertl *et al.*, 2003; Bosi and Skogby, 2013; Pieczka *et al.*, 2018; Sęk *et al.*, 2022), the sample studied shows similar chemical composition and structural parameters (Table 7). Oxy-dravite from the quartz vein located in a granitic gneiss of the Kowary gneiss series (Wołowa Góra Mountain; Pieczka *et al.*, 2018), has comparable values of Si^{4+}, Ti^{4+} and F^{-}. However, the Beluga oxy-dravite has lower contents of Ca^{2+} (0.08 *vs.* 0.15 apfu) and Mg^{2+} (1.89 *vs.* 2.53 apfu) but higher contents of Fe^{2+} (0.15 *vs.* 0.04 apfu), Na^{+} (0.88 *vs.* 0.80 apfu) and Al$_{tot}^{3+}$ (7.06 *vs.* 6.36 apfu).

Structurally, the X-site of the Beluga and holotype tourmalines is occupied predominantly by Na with minor amounts of Ca and vacancies, supported by the mean <X–O> bond length of 2.673 Å. The comprehensive review of Ertl and Tillmanns (2012) showed that <X–O> values range between 2.67 and 2.68 Å for tourmalines with Na = 1 apfu, whereas solely calcic tourmalines are characterised by shorter (<2.63 Å) <X–O> distances (e.g. Ertl *et al.*, 2006; Scribner *et al.*, 2021; Bosi *et al.*, 2022); on the other hand, X-vacant tourmalines typically feature longer <X–O> distances (Selway *et al.*, 1998; Ertl *et al.*, 2005; Bosi and Lucchesi, 2007; Bačík *et al.*, 2015).

In comparison with solely calcic tourmalines, the mean bond length <X–O> of oxy-dravite is longer. The B-site is characterised by the mean <B–O> bond length of 1.375 Å, which is considered to be evidence of full occupancy by B (Bosi and Lucchesi, 2007; Pieczka *et al.*, 2018). The Y-site is occupied mainly by Mg and Al, in a lesser amount also by Fe and Ti. The mean bond length for <Y–O> is 1.999 Å, only slightly lower than in the ^{Y}Fe^{3+}-rich oxy-dravites studied by Bosi and Skogby (2013) and Pieczka *et al.* (2018). The ionic radius value of Fe^{3+} in tourmaline
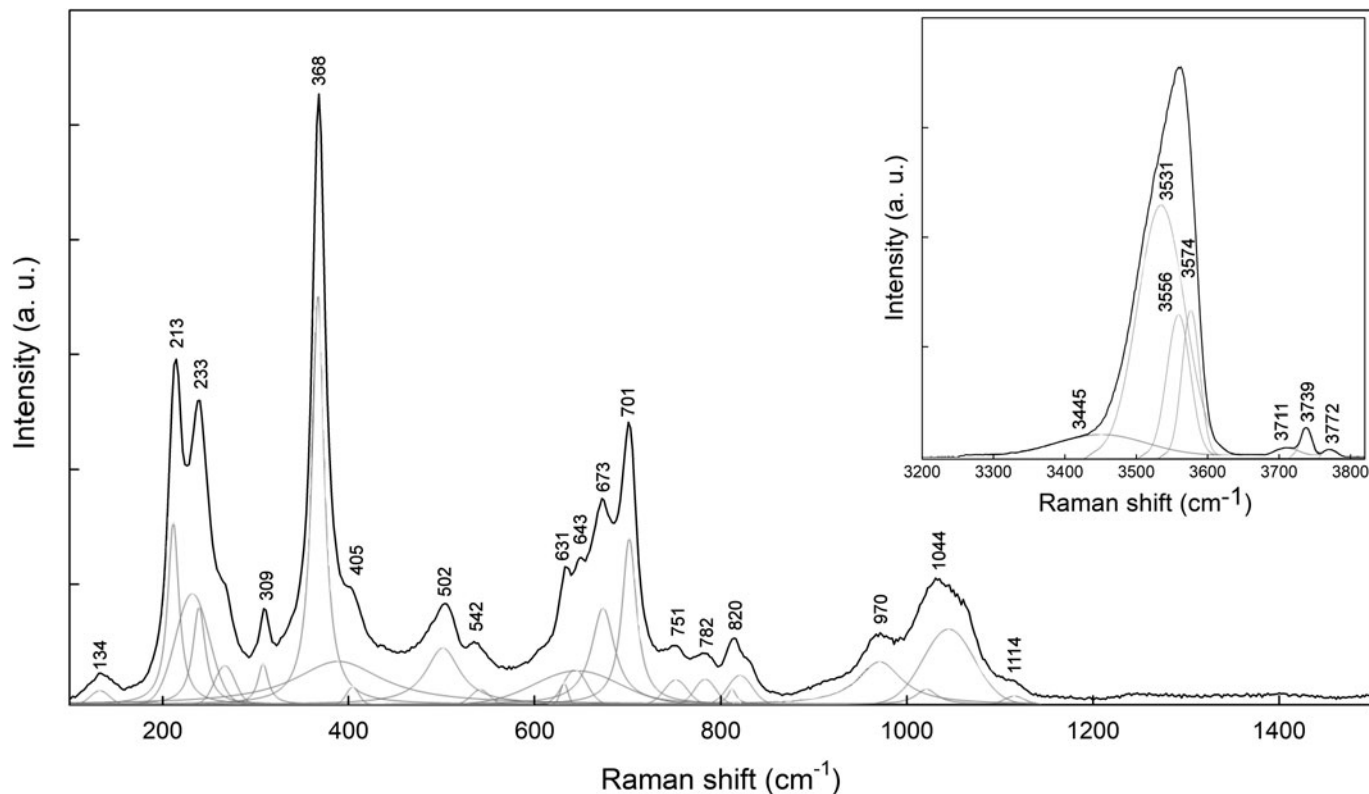
Figure 4. Polarised Raman spectra (black) and the main fitted bands (grey) for the Beluga oxy-dravite (orientation || *c*).

(0.697 Å; Bosi and Lucchesi, 2007) is between those for Mg and Al (0.723 and 0.547 Å) and is much lower than that of Fe^{2+} (0.778 Å); the presence of $^YFe^{3+}$ therefore has a much smaller effect on <Y–O> lengths than the dominant $^{Y,Z}(Al, Mg)$ disorder. The Y–O1 distance is one of the shortest reported in tourmaline (e.g. Bačík, 2018) and indicates high $^WO^{2-}$ content. The Z-site is occupied by Al and minor amount of Mg. The slightly extended mean <Z–O> bond length of 1.928 Å (ideally ~1.906 Å; Bosi and Andreozzi, 2013) indicates, along with the mismatch in the size of the cations occupying the Z-site, Al–Mg disorder among the Y- and Z-sites (Grice and Ercit, 1993; Hawthorne, 1996 and 2002; Bosi and Luccesi, 2007; Bosi and Skogby, 2013; Pieczka *et al.*, 2018). The arrangement of Mg and Al at the Y- and Z-sites is, in the case of oxy-dravite, closely connected with the presence of O^{2-} at the W-site and its incorporation is controlled by the following substitution: $3^YMg^{2+} + 2^ZAl^{3+} + {}^W(OH)^{1-} \leftrightarrow 3^YAl^{3+} + 2^ZMg^{2+} + {}^WO^{2-}$ (Hawthorne, 1996; Henry *et al.*, 2011; Bosi and Skogby, 2013). The short-range bond-valence requirements at the W-site (O1) suggest two possibilities of end-members if fully occupied by $^WO^{2-}$: an unstable $^Y(Al + 2Mg)-{}^W(O^{2-})$ configuration (or substitution) and the preferred stable configuration $^Y(3Al)-{}^W(O^{2-})$ or $^Y(2Al + Mg)-{}^W(O^{2-})$ (Hawthorne, 1996, 2002; Bosi and Skogby, 2013). It is noteworthy that in tourmalines with significant Fe, the structure can be stabilised (and the <Y–O> distance reduced, see discussion of ionic radii above) by simple oxidation of Fe^{2+} to Fe^{3+} (exchange mechanism $3^YFe^{2+} + 2^ZFe^{3+} + {}^W(OH)^{1-} \leftrightarrow 3^YFe^{3+} + 2^ZFe^{2+} + {}^WO^{2-}$) without necessity of physical octahedral cation disorder.

According to Bosi and Lucchesi (2007), there are structural-stability limits for tourmaline-supergroup minerals which can be expressed by the maximum difference of ca. 0.15 Å

between <Y–O> and <Z–O>. In Fig. 6, we compare the <Y–O> and <Z–O> average bond lengths for natural oxy-dravites to theoretical values of some ordered and disordered ideal end-members (marked as stars in Fig. 6) calculated using the ionic radii method (Bosi and Lucchesi, 2007). The Y-site ordered form of oxy-dravite with $^YAl_3{}^Z(Al_4Mg_2)$ configuration falls into the unstable field; in contrast, both the Z-site ordered and Y,Z-site disordered forms of oxy-dravite fit the stability field (Fig. 6).

The structure of oxy-dravite is influenced significantly by the presence of $^WO^{2-}$, unlike dravite, so it is necessary to consider short-range bond-valence requirements around O1 (Bosi and Skogby, 2013). As the configuration $^YMg^YMg^YMg-{}^WO$ is unstable due to underbonding of the O1 anion, the incorporation of $^WO^{2-}$ requires disorder of Mg and Al between the Y and Z sites (expressed by the substitution $2^YMg^{2+} + {}^ZAl^{3+} + {}^W(OH)^{1-} \leftrightarrow 2^YAl^{3+} + {}^ZMg^{2+} + {}^WO^{2-}$) to keep the structure stable and electroneutral.

Petrogenesis of Beluga oxy-dravite

The Beluga occurrence of oxy-dravite in calc-silicate pods associated with marbles represents another example of its formation in Mg-rich environments related to metamorphism of a sedimentary sequence (Belley *et al.*, 2017). Here, marine dolomitic argillaceous marl was influenced by (B,Cl)-rich fluids, probably proximally-derived from mineral breakdown reactions, in the retrograde stage of metamorphism. The localised nature of retrograde mineralisation in scapolite-bearing calc-silicate pods at Beluga and in its vicinity suggest relatively closed system processes except for the addition or loss of volatiles (Belley *et al.*, 2017). The textural relationship between corundum and oxy-dravite indicates
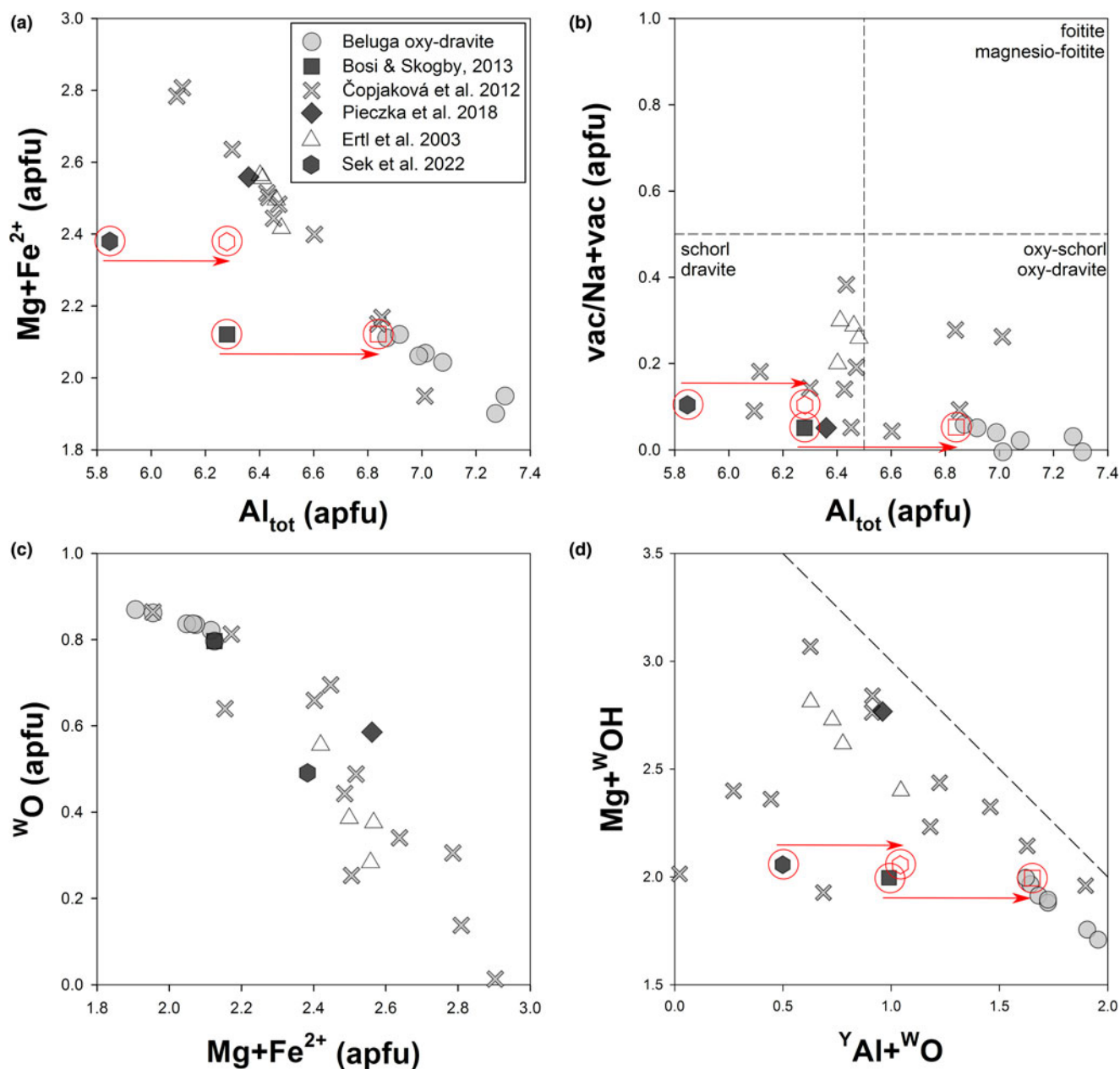
Figure 5. Composition of the Beluga oxy-dravite for X,Y,Z,W,V sites compared to compositions from other studies (Ertl *et al.*, 2003; Čopjaková *et al.*, 2012; Bosi and Skogby, 2013; Pieczka *et al.*, 2018; Sęk *et al.*, 2022). Red arrows and symbols indicate position shift in Fe^{3+}-bearing tourmalines if ($Al_{tot} + Fe^{3+}$) is used instead of Al_{tot}.

that oxy-dravite could have formed (1) simultaneously with corundum or (2) after corundum. Breakdown of phlogopite to muscovite and other phases (Belley, unpublished data 2023), possibly subsequent to corundum genesis, could provide Mg and other elements required to form oxy-dravite. The volume of oxy-dravite at Beluga is very low, therefore trace amounts of B in phlogopite could be sufficient if the volume of phlogopite destroyed in retrograde metamorphism is sufficient. Alternatively, B could be sourced from the breakdown of an unknown mineral phase.

The purity of Beluga oxy-dravite with regard to elevated Fe, Ti and F observed at other localities could be explained by: (1) the relatively low concentrations of Fe and Ti in Beluga calc-silicate rock relative to other oxy-dravite host rocks (i.e. Pieczka *et al.*, 2018); (2) conservation of these elements in phlogopite, which

is abundant in unaltered phlogopite–oligoclase domains contiguous to corundum- and oxy-dravite-bearing zones, reducing the availability of these elements to oxy-dravite growing in the corundum-bearing domain (see Belley *et al.*, 2017); and/or (3) in the case of oxy-dravite formation subsequent to phlogopite breakdown in the corundum-bearing domain, the preferential incorporation of Fe and Ti in pyrrhotite and Ti-oxide, respectively. Beluga oxy-dravite's high Mg/Fe values may reflect the presence of reduced S during retrograde metamorphism (forming pyrrhotite), where Fe would strongly partition to pyrrhotite relative to silicates (see the related discussion relating to Fe partitioning in metamorphic pyrrhotite and spinel in metacarbonates in the same field area; Belley and Groat, 2019). Ultimately, the exact factors that have resulted in the formation of near end-

Table 7. Comparison of mean bond lengths of oxy-dravite from different studies.

	Beluga	Bosi and Skogby, (2013)	Pieczka *et al.* (2018)	Ertl *et al.* (2003)	Sęk *et al.* (2022)
<T–O>	1.621	1.619	1.617	1.620	1.620
<Z–O>	1.928	1.933	1.925	1.926	1.933
<Y–O>	1.999	2.004	2.015	2.010	2.031
<X–O>	2.673	2.683	2.676	2.682	2.689
<B–O>	1.376	1.375	1.374	1.374	1.373
O1–H1	n.d.	n.d.	0.970	n.d.	n.d.
O3–H3	0.925	0.850	0.920	n.d.	n.d.

'n.d.' – not determined

member oxy-dravite are difficult to establish with high accuracy due to the complex metamorphic history, large grain sizes, and extensive retrograde overprints at the Beluga sapphire occurrence.

The predominance of Na over Ca and K at the X site correlates with an end-member albite composition in plagioclase in this zone (Belley *et al.*, 2017) which matches the experimental results of von Goerne *et al.* (2011). The low amounts of vacancies found in the Beluga oxy-dravite indicate high ionic strength of the fluid phase (von Goerne *et al.*, 2011) equivalent to ca. 0.33–0.40 mol/l (fluid at 300–400°C; Dutrow and Henry, 2016). Berryman *et al.*, (2016) showed that Ca-rich tourmalines are expected to form at

low P and high T conditions in Ca-rich rocks; other conditions (low T, high P) show tourmaline preference for Na whereas Ca is partitioned to the coexisting fluid. These data correspond well with the Beluga tourmaline-bearing assemblage (albite + muscovite + calcite) which formed at relatively low P,T conditions; the presence of oxy-dravite therefore indicates high Na (±K) in acidic (tourmaline is not stable under alkaline conditions) fluid.

Implications for oxy-dravite occurrence

Pieczka *et al.* (2018) reported that the main petrogenetic environments of oxy-dravites are aluminous metapelites and metapsammites (e.g. Bosi and Skogby, 2013; Čopjaková *et al.*, 2012; Ertl *et al.*, 2003; Pieczka *et al.*, 2018), low-Ca ultramafics (Sęk *et al.*, 2022), and (Cr,V)-rich metasediments (e.g. Bosi and Lucchesi, 2004; Cempírek *et al.*, 2013).

The fourth, rather rare type of oxy-dravite occurrence is in metamorphosed calcareous sediments and limestones. It was reported in metaevaporite layers in dolomite marble near Prosetín, Czech Republic (Bačík *et al.*, 2012) and at contacts of calcite–dolomite marbles with metamorphic rocks found at the Blažkov and Třebenice localities, Czech Republic (Krmíček *et al.*, 2021). The Beluga occurrence represents a rather unique (near-end-member composition, unique association with corundum) occurrence from this type of environment. The polyphase
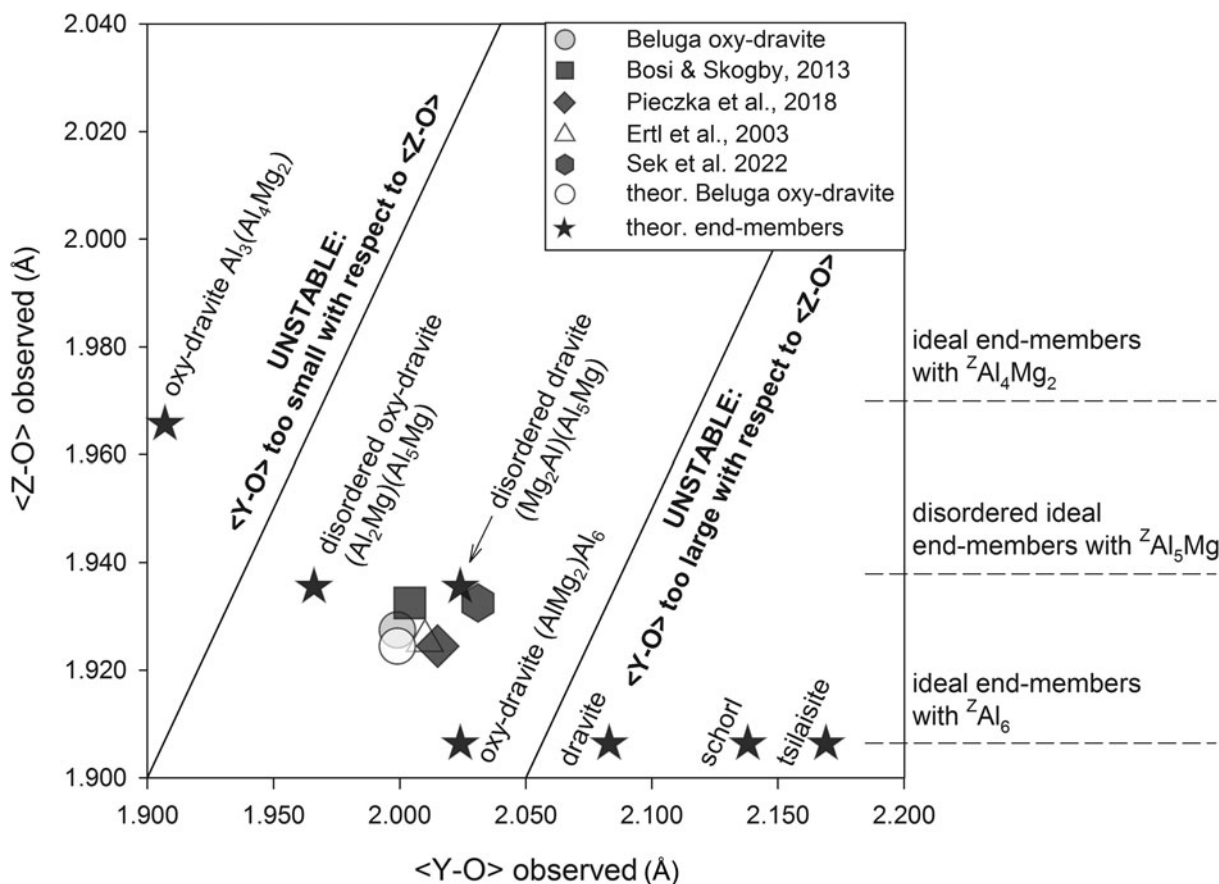

Figure 6. Mean atom distances of the Y- and Z-sites for the Beluga oxy-dravite compared to published data, theoretical values, and tourmaline structural stability limits (calculations and stability limits after Bosi and Lucchesi, 2007). The diagram shows the general similarity of average octahedral bond lengths despite high $^Y Fe^{3+}$ in some data (Bosi and Skogby, 2013; Sęk *et al.*, 2022) and shift of the Beluga Fe-free composition <Y–O> towards the theoretical value for the $^Y(Al_2Mg)(Al_5Mg)$ configuration.

evolution of its host rock was the key to the observed extreme depletion in typical minor elements (Fe, Cr, V, Ti, Ca and F) that are found in oxy-dravite worldwide.

References

Bačík P. (2015) Cation ordering at octahedral sites in schorl-dravite series tourmalines. *The Canadian Mineralogist*, **53**, 571–590.

Bačík P. (2018) The crystal-chemical autopsy of octahedral sites in Na-dominant tourmalines: Octahedral metrics model unconstrained by the Y, Z-site disorder assignment. *Journal of Geosciences*, **63**, 137–154.

Bačík P., Uher P., Cempírek J. and Vaculovič T. (2012) Magnesian tourmalines from plagioclase–muscovite–scapolite metaevaporite layers in dolomite marble near Prosetín (Olešnice Unit, Moravicum, Czech Republic). *Journal of Geosciences*, **57**, 143–153.

Bačík P., Ertl A., Števko M., Giester G. and Sečkár P. (2015) Acicular zoned tourmaline (magnesio-foitite to foitite) from a quartz vein near Tisovec, Slovakia: The relationship between crystal chemistry and acicular habit. *The Canadian Mineralogist*, **53**, 221–234.

Belley P.M. and Groat L.A. (2019) Metacarbonate-hosted spinel on Baffin Island, Nunavut, Canada: Insights into the origin of gem spinel and cobalt-blue spinel. *The Canadian Mineralogist*, **57**, 147–200.

Belley P.M. and Groat L.A. (2020) Metamorphosed carbonate platforms and controls on the genesis of sapphire, gem spinel, and lapis lazuli: Insight from the Lake Harbour Group, Nunavut, Canada and implications for gem exploration. *Ore Geology Reviews*, **116**, 103259.

Belley P.M., Dzikowski T.J., Fagan A., Cempírek J., Groat L.A., Mortensen J.K., Fayek M., Giuliani G., Fallick A.E. and Gertzbein P. (2017) Origin of scapolite-hosted sapphire (corundum) near Kimmirut, Baffin Island, Nunavut, Canada. *The Canadian Mineralogist*, **55**, 669–699.

Berryman E.J., Wunder B., Rhede D., Schettler G., Franz G. and Heinrich W. (2016) P–T–X controls on Ca and Na distribution between Mg–Al tourmaline and fluid. *Contributions to Mineralogy and Petrology*, **171**, 1–14.

Bosi F. (2013) Bond-valence constraints around the O1 site of tourmaline. *Mineralogical Magazine*, **77**, 343–351.

Bosi F. and Andreozzi G.B. (2013) A critical comment on Ertl et al. (2012): "Limitations of Fe^{2+} and Mn^{2+} site occupancy in tourmaline: Evidence from Fe^{2+}- and Mn^{2+}-rich tourmaline". *American Mineralogist*, **98**, 2183–2192.

Bosi F. and Lucchesi S. (2004) Crystal chemistry of the schorl-dravite series. *European Journal of Mineralogy*, **16**, 335–344.

Bosi F. and Lucchesi S. (2007) Crystal chemical relationships in the tourmaline group: Structural constraints on chemical variability. *American Mineralogist*, **92**, 1054–1063.

Bosi F. and Skogby H. (2013) Oxy-dravite, $Na(Al_2Mg)(Al_5Mg)(Si_6O_{18})$ $(BO_3)_3(OH)_3O$, a new mineral species of the tourmaline supergroup. *American Mineralogist*, **98**, 1442–1448.

Bosi F., Reznitskii L.Z. and Sklyarov E.V. (2013) Oxy-vanadium-dravite, $NaV_3(V_4Mg_2)(Si_6O_{18})(BO_3)_3(OH)_3O$: Crystal structure and redefinition of the "vanadium-dravite" tourmaline. *American Mineralogist*, **98**, 501–505

Bosi F., Reznitskii L.Z., Hålenius U. and Skogby H. (2017a) Crystal chemistry of Al-V-Cr oxy-tourmalines from Sludyanka complex, Lake Baikal, Russia. *European Journal of Mineralogy*, **29**, 457–472.

Bosi F., Skogby H., Ciriotti M. E., Gadas P., Novák M., Cempírek J., Všianský D. and Filip J. (2017b) Lucchesiite, $CaFe_3^{2+}Al_6(Si_6O_{18})$ $(BO_3)_3(OH)_3O$, a new mineral species of the tourmaline supergroup. *Mineralogical Magazine*, **81**, 1–14.

Bosi F., Biagioni C., Pezzotta F., Skogby H., Hålenius U., Cempírek J., Hawthorne F.C., Lussier A. J., Abdu Y.A., Day M.C., Fayek M., Clark Ch.M., Grice J.D. and Henry D.J. (2022) Uvite, $CaMg_3(Al_5Mg)(Si_6O_{18})$ $(BO_3)_3(OH)_3(OH)$, a new, but long-anticipated mineral species of the tourmaline supergroup from San Piero in Campo, Elba Island, Italy. *Mineralogical Magazine*, **86**, 767–776.

Bruker (2007) *SAINT*. Bruker AXS Inc., Madison, Wisconsin, USA.

Cempírek J., Houzar S., Novák M., Groat L.A., Selway J.B. and Šrein V. (2013) Crystal structure and compositional evolution of vanadium-rich oxy dravite from graphite quartzite at Bítovánky, Czech Republic. *Journal of Geosciences*, **58**, 149–162.

Clark C.M., Hawthorne F.C. and Ottolini L. (2011) Fluor-dravite, $NaMg_3Al_6Si_6O_{18}(BO_3)_3(OH)_3F$, a new mineral species of the tourmaline group from the Crabtree emerald mine, Mitchell County, North Carolina: description and crystal structure. *The Canadian Mineralogist*, **49**, 57–62.

Čopjaková R., Škoda R. and Vašinová-Galiová M. (2012) „Oxy-dravit" z turmalinitů krkonošsko-jizerského krystalinika. *Bulletin Mineralogicko-Petrologického Oddělení Národního Muzea v Praze*, **20**, 37–46.

Corrigan D., Pehrsson S., Wodicka N. and de Kemp E. (2009) The Paleoproterozoic Trans-Hudson Orogen: a prototype of modern accretionary processes. *Geological Society London, Special Publications*, **327**, 457–479.

Drivenes K. (2022) Sn-rich tourmaline from the Land´s End granite, SW England. *Journal of Geosciences*, **67**, 173–189.

Duchoslav M., Marks M.A.W., Drost K., McCammon C., Marschall H.R., Wenzel T. and Markl G. (2017) Changes in tourmaline composition during magmatic and hydrothermal processes leading to tin-ore deposition: The Cornubian Batholith, SW England. *Ore Geology Reviews*, **83**, 215–234.

Dutrow B.L. and Henry D.J. (2016) Fibrous tourmaline: A sensitive probe of fluid compositions and petrogenetic environments. *The Canadian Mineralogist*, **54**, 311–335.

Ertl A. and Tillmanns E. (2012) The [9]-coordinated X site in the crystal structure of tourmaline-group minerals. *Zeitschrift für Kristallographie – Crystalline Materials*, **227**, 456–459.

Ertl A., Hughes J.M., Brandstätter F., Dyar M.D. and Prasad P.S.R. (2003) Disordered Mg-bearing olenite from a granitic pegmatite at Goslarn, Austria: A chemical, structural, and infrared spectroscopic study. *The Canadian Mineralogist*, **41**, 1363–1370.

Ertl A., Rossman G.R., Hughes J.M., Prowatke S. and Ludwig T. (2005) Mn-bearing "oxy-rossmaite" with tetrahedrally coordinated Al and B from Austria: Structure, chemistry, and infrared and optical spectroscopic study. *American Mineralogist*, **90**, 481–487.

Ertl A., Hughes J.M., Prowatke S., Ludwig T., Prasad P.S.R., Brandstätter F., Körner W., Schuster R., Pertlik F. and Marschall H. (2006) Tetrahedrally coordinated boron in tourmalines from the liddicoatite-elbaite series from Madagascar: Structure, chemistry, and infrared spectroscopic studies. *American Mineralogist*, **91**, 1847–1856.

Ertl A., Henry D.J. and Tillmanns E. (2018) Tetrahedral substitutions in tourmaline: a review. *European Journal of Mineralogy*, **30**, 465–470.

Fantini C., Tavares M.C., Krambrock K., Moreira R.L. and Righi A. (2014) Raman and infrared study of hydroxyl sites in natural uvite, fluor-uvite, magnesio-foitite, dravite and elbaite tourmalines. *Physics and Chemistry of Minerals*, **41**, 247–254.

Foit F.F. and Rosenberg P.E. (1979) The structure of vanadium-bearing tourmaline and its implications regarding tourmaline solid solutions. *American Mineralogist*, **64**, 788–798.

Gadas P., Novák M., Cempírek J., Filip J., Galiová M.V., Groat L.A., and Všianský D. (2014) Mineral assemblages, compositional variation, and crystal structure of feruvitic tourmaline from a contaminated anatectic pegmatite at Mirošov near Strážek, Moldanubian Zone, Czech Republic. *The Canadian Mineralogist*, **52**, 285–301.

Gagné O.C. and Hawthorne F.C. (2015) Comprehensive derivation of bond-valence parameters for ion pairs involving oxygen. *Acta Crystallographica*, **B71**, 562–578.

Grice J.D. and Ercit T.S. (1993) Ordering of Fe and Mg in the tourmaline crystal structure: The correct formula. *Neues Jahrbuch für Mineralogie – Abhandlungen*, **165**, 245–266.

Hawthorne F.C. (1996) Structural mechanisms for light-element variations in tourmaline. *The Canadian Mineralogist*, **34**, 123–132.

Hawthorne F.C. (2002) Bond-valence constraints on the chemical composition of tourmaline. *The Canadian Mineralogist*, **40**, 789–797.

Hawthorne F.C., MacDonald D.J. and Burns P.C. (1993) Reassignment of cation site occupancies in tourmaline: Al–Mg disorder in the crystal structure of dravite. *American Mineralogist*, **78**, 265–270.

Henry D.J. and Dutrow B.L. (1996) Chapter 10. Metamorphic tourmaline and its petrologic applications. Pp. 503–558 in *Boron: Mineralogy, Petrology, and Geochemistry* (L.M. Anovitz and E.S. Grew, editors). Mineralogical Society of America and the Geochemical Socitety, Chantilly, Virginia, USA.

Henry D.J., Sun H., Slack J.F. and Dutrow B.L. (2008) Tourmaline in meta-evaporites and highly magnesian rocks: perspectives from Namibian tourmalinites. *European Journal of Mineralogy*, **20**, 5, 889–904.

Henry D.J., Novák M., Hawthorne F.C., Ertl A., Dutrow B.L., Uher P. and Pezzotta F. (2011) Nomenclature of the tourmaline-supergroup minerals. *American Mineralogist*, **96**, 895–913.

Hogarth D.D. (1971) Lapis lazuli near Lake Harbour, Southern Baffin Island, Canada. *Canadian Journal of Earth Sciences* **8**, 1210–1217.

Hovestreydt E. (1983) On the atomic scattering factor for O^{2-}. *Acta Crystallographica Section A: Foundations of Crystallography*, **39**, 268–269.

Krmíček L., Novák M., Trumbull R.B., Cempírek J. and Houzar S. (2021) Boron isotopic variations in tourmaline from metacarbonates and associated calc-silicate rocks from the Bohemian Massif: Constraints on boron recycling in the Variscan orogen. *Geoscience Frontiers*, **12**, 219–230.

Lepage L. and Rohtert W. (2006) Ultraviolet mineral prospecting for sapphire on Baffin Island, Nunavut, Canada. Gemological Research Conference. *Gems and Gemology*, **42**, 155–156.

MacDonald D. J. and Hawthorne F. C. (1995) The crystal chemistry of Si↔Al substitution in tourmaline. *The Canadian Mineralogist*, **33**, 849–858.

Mandarino J.A. (1981) The Gladstone-Dale relationship: Part IV. The Compatibility concept and its application. *The Canadian Mineralogist*, **19**, 441–450.

Novák M., Povondra P. and Selway J.B. (2004) Schorl-oxy-schorl to dravite-oxy-dravite tourmaline from granitic pegmatites; examples from the Moldanubicum, Czech Republic. *European Journal of Mineralogy*, **16**, 323–333.

Ottolini L., Cámara F. and Bigi S. (2000) An investigation of matrix effects in the analysis of fluorine in humite-group minerals by EMPA, SIMS, and SREF. *American Mineralogist*, **85**, 89–102.

Pieczka A., Ertl A., Sek M.P., Twardak D., Zelek S., Szeleg E. and Giester G. (2018) Oxy-dravite from Wolowa Góra Mountain, Karkonosze massif, SW Poland: Crystallochemical and structural studies. *Mineralogical Magazine*, **82**, 913–928.

Scott D.J. (1997) Geology, U-Pb, and Pb-Pb geochronology of the Lake Harbour area, southern Baffin Island: Implications for the Paleoproterozoic tectonic evolution of northeastern Laurentia. *Canadian Journal of Earth Sciences* **34**, 140–155.

Scribner E.D., Cempírek J., Groat L.A., Evans R.J., Biagioni C., Bosi F., Dini A., Hålenius U., Orlandi P. and Pasero M. (2021) Magnesio-lucchesiite, $CaMg_3Al_6 (Si_6O_{18})(BO_3)_3(OH)_3O$, a new species of the tourmaline supergroup. American Mineralogist: *Journal of Earth and Planetary Materials*, **106**, 862–871.

Sęk M.P., Włodek A., Stachowitz M., Woźniak K. and Pieczka A. (2022) Magnesio-lucchesiite from the Kowary vicinity, Karkonosze Mountains, SW Poland: the third occurrence worldwide. *Mineralogical Magazine*, **87**, 60–68

Selway J.B., Novák M., Hawthorne F.C., Černý P., Ottolini L. and Kyser T.K. (1998) Rossmanite, $\Box(LiAl_2)Al_6(Si_6O_{18})(BO_3)_3(OH)_4$, a new alkali-deficient tourmaline: Description and crystal structure. *American Mineralogist*, **83**, 896–900.

Sheldrick G.M. (2008) A short history of SHELX. *Acta Crystallographica*, **A64**, 112–122.

Sheldrick G.M. (2015) Crystal structure refinement with SHELXL. *Acta Crystallographica*, C71, 3–8.

St-Onge M.R., Wodicka N. and Ijewliw O. (2007) Polymetamorphic evolution of the Trans-Hudson Orogen, Baffin Island, Canada: Integration of petrological, structural and geochronological data. *Journal of Petrology* **48**, 271–302.

von Goerne G., Franz G. and van Hinsberg V.J. (2011) Experimental determination of Na–Ca distribution between tourmaline and fluid in the system $CaO–Na_2O–MgO–Al_2O_3–SiO_2–B_2O_3–H_2O$. *The Canadian Mineralogist*, **49**, 137–152.

Watenphul A., Burgdorf M., Schlüter J., Horn I., Malcherek T. and Mihailova B. (2016a) Exploring the potential of Raman spectroscopy for crystallochemical analyses of complex hydrous silicates: II. Tourmalines. *American Mineralogist*, **101**, 970–985.

Watenphul A., Schlüter J., Bosi F., Skogby F., Malcherek T. and Mihailova B. (2016b) Influence of the octahedral cationic-site occupancies on the framework vibrations of Li-free tourmalines, with implications for estimating temperature and oxygen fugacity in host rocks. *American Mineralogist*, **101**, 2554–2563.

Watenphul A., Malcherek T., Wilke F.D.H., Schlüter J. and Mihailova B. (2017) Composition–thermal expandability relations and oxidation processes in tourmaline studied by in situ Raman spectroscopy. *Physics and Chemistry of Minerals*, **44**, 735–748.